Annals of Nuclear Energy 236 (2026) 112420

Contents lists available at ScienceDirect

Annals of Nuclear Energy

journal homepage: www.elsevier.com/locate/anucene

Analysis of turbulence-induced crossflow and coolant mixing under various flow interventions in rod bundle geometries

Prince Amoah [a,d], Vincent Yao Agbodemegbe [a,b], Edward Shitsi [a,b,c,*], Emmanuel Ampomah-Amoako [a,d]

[a] Department of Nuclear Engineering, School of Nuclear and Allied Sciences, College of Basic and Applied Sciences, University of Ghana, Accra, Ghana
[b] Ghana Atomic Energy Commission, Accra, Ghana
[c] Nuclear Power Institute, Ghana Atomic Energy Commission, Accra, Ghana
[d] Nuclear Regulatory Authority, Accra, Ghana

ARTICLE INFO

Keywords:
Flow intervention
Turbulence
Cross flow
Rod bundles
Mixing coefficient

ABSTRACT

In recent times efforts have been made to understand turbulence-induced crossflow and coolant mixing in fuel rod bundles. This phenomenon in nuclear reactors is essential for optimizing heat removal. This study investigates the contribution of fuel bundles with split vane, swirl vane, spacer grid and no spacer grid to the development of secondary flows, turbulence, and crossflow. High-fidelity simulations were employed to quantify axial and lateral flow redistribution, turbulent kinetic energy (TKE) evolution, dissipation behaviour, vorticity and velocity distribution patterns across bundle subchannels. Results show that vane-type spacers substantially intensify crossflow by generating strong streamwise vortices that persist downstream, with swirl vanes producing the most sustained mixing effects. Turbulence metrics reveal elevated TKE, localized production peaks, and enhanced dissipation in all vane-equipped configurations, consistent with classical energy cascade behaviour. Collectively, the findings demonstrate that fuel rod bundles equipped with flow mixing interventions induce turbulence which significantly improves crossflow and coolant mixing, providing a foundation for improved crossflow correlation development and supporting the design of next-generation high-performance rod bundle assemblies.

1. Introduction

Nuclear power plants contribute about 16% of the world's electricity and this is by virtue of the fission reaction of the nuclear fuels liberating a tremendous amount of energy (Pioro & Duffey, 2019; World Energy Outlook 2023 – *Event* – *IEA*, n.d.). The heat released during the nuclear fission process is absorbed by coolants that circulate around these fuel rods or plates. The nature of the flow of the coolant directly influences the effectiveness of the heat transfer as well as inter-channel mixing between sub-channels. For effective transfer and uniform distribution of the heat, the flow of the coolant must be Turbulent. In some nuclear reactors, fuel assemblies are designed with flow interventions to induce turbulence. Owing to the significant advancements in CFD applications, interest in research to better understand the mechanisms of turbulent mixing has increased. This study presents a numerical analysis on the turbulence-induced crossflow and coolant mixing effect for four different rod bundle geometries. Fig. 1 shows a cylindrical fuel assembly supported by spacer grid with mixing vane.

1.1. Turbulent intensity

Turbulent intensity (I) is a dimensionless parameter that is used to quantify the degree of turbulence in the flow of a fluid. It is defined as the ratio of the root-mean-square (RMS) of turbulent velocity fluctuations ($\acute{u}_{rms}$) to the mean flow velocity ($\overline{u}$): Mathematically represented as:

$$I = \frac{\acute{u}_{rms}}{\overline{u}} \times 100\% \tag{1}$$

where,

* Corresponding author.
E-mail addresses: amprince77@gmail.com (P. Amoah), vincevalt@googlemail.com (V.Y. Agbodemegbe), edwardshitsi@yahoo.com (E. Shitsi), emmanuel.amoako@nra.gov.gh (E. Ampomah-Amoako).

https://doi.org/10.1016/j.anucene.2026.112420
Received 16 December 2025; Received in revised form 6 April 2026; Accepted 2 May 2026
Available online 12 May 2026
0306-4549/© 2026 Elsevier Ltd. All rights are reserved, including those for text and data mining, AI training, and similar technologies.

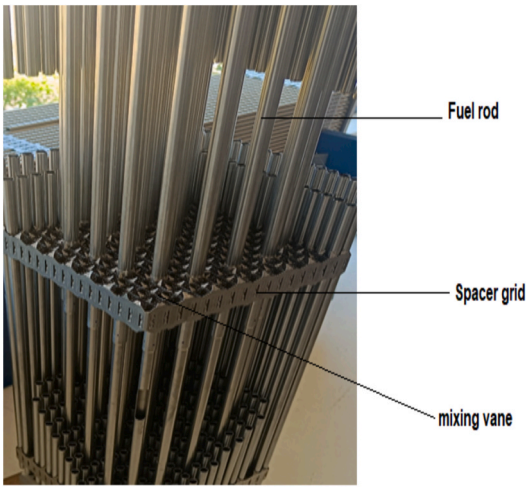


Fig. 1. Fuel Assembly with cylindrical fuel rods and spacer grid.

$$\acute{u}_{rms} = \sqrt{\frac{1}{3}(u'^2 + v'^2 + w'^2)} \tag{2}$$

where u', v' *and* w' are velocity fluctuations in the streamwise, transverse and spanwise directions and $\bar{u}$ is the mean flow velocity (Conboy et al., 2013; J. Lee et al., 2019).

In rod bundles, turbulent intensity is critical for determining the mixing enhancement in the core of the reactor. A higher turbulent intensity (I) promotes lateral momentum/energy exchange between subchannels, reducing temperature gradients and preventing hotspots (Möller, 1992). This is due to increased convective heat transfer which correlates with the Stanton number (*St*), thus a better heat transfer from fuel rods to coolant. The use of structural interventions is expected to increase the turbulent intensity.

In PWRs, although the spacer grid's primary function is to secure the fuel rods mechanically in place, it is connected to a variety of flow deflectors in order to increase the turbulent intensity and subchannel flow mixing.

1.2. Subchannel flow mixing

Subchannel flow mixing plays a crucial role in maintaining uniform temperature distribution, preventing localized hotspots, and improving the overall heat transfer efficiency of the reactor core. The driving forces behind subchannel mixing include pressure gradients, turbulent diffusion, and the effects of structural intervention, which enhance crossflow. Structural interventions like mixing vanes are attached to spacer grids to create a swirling motion in the flow, which passively improves mixing in the sub-channels. Spacer grids are typically used to mechanically support the fuel rods in a long, straight channel, but they can also be used to prevent hot spots and manage flow-induced vibration (Hainoun et al., 2014; Xiong et al., 2020; Feldman, 2010). The mass flow rate is calculated from one subchannel i to another subchannel j per unit length as:

$$m_{ij} = \mu^{+}\rho U_{mj} \tag{3}$$

where ρ represents the density, U_{mj}, is the mean axial velocity in subchannel i, and μ^{+} a mixing coefficient that gives the fraction of mass per unit length flowing from subchannel i to j.

The mixing flow rate m_{ij} is generally expressed in non-dimensional form as:

$$m_{ij}^{+} = m_{ij}/\mu \tag{4}$$

The pressure difference between adjacent sub channels ΔP_{ij} is related to the local crossflow velocity between the sub- channels i and j as

$$\Delta Pij = \frac{K\rho\mu^2}{2} \text{(Feldman, 2010; Xiong et al., 2020)} \tag{5}$$

Crossflow in subchannel bundles is largely governed by lateral momentum exchange driven by secondary flow structures and pressure gradients. Turbulent dissipation charge acts to attenuate the strength of these lateral jets or vortical motions by depleting turbulent energy from the system. However, as turbulent dissipation increases downstream, the swirling structures weaken, and crossflow intensity diminishes. On the other hand, in low-dissipation regions, crossflow can remain relatively strong and coherent. Thus, a balance between turbulent production and dissipation is essential in determining the sustainability and pattern of crossflow, and controlling this balance through geometry and grid design is a key strategy in thermal–hydraulic optimization of nuclear reactor cores.

As in the case of fluid dynamics, the fundamental governing equations for continuity, momentum and energy is computed for flow of the coolant in rod bundles. There are two ways to express the conservation laws for a continuum: Eulerian and Lagrangian. According to the Eulerian method, a given volume is a section of space across which material can move. A specific volume in the Lagrangian technique denotes a section of the body's material, allowing an observer to track the material as it travels through space-enhanced (Kaptsov et al., 2018). For a finite control volume fixed in space as shown in Fig. 2. If the flow velocity is v and the elemental surface area is dS and dV is the elemental volume inside the control volume, then for continuum conservation,

$$\frac{\partial}{\partial t}\iiint_{v}\rho dV + \iint_{S}\rho V.dS = 0 \tag{6}$$

Also written as, $\frac{\partial\rho}{\partial t} + \nabla \bullet (\rho v) = 0$ where ρ is the density and v is the continuum velocity.

For the conservation of momentum, Newton's second law is applied to the flow of the fluid resulting in equation (7).

$$-\iint_{S}\rho dS + \iiint_{v}\rho f dV + F_{viscous} = \frac{\partial}{\partial t}\iiint_{v}\rho V dV + \iint_{S}(\rho V \bullet dS)V \tag{7}$$

Which is written in three dimensions as,

$$\begin{aligned}\frac{\partial(\rho u)}{\partial t} + \nabla \bullet (\rho u V) &= -\frac{\partial\rho}{\partial x} + \rho f_x + (F_x)_{viscous}\frac{\partial(\rho v)}{\partial t} + \nabla \bullet (\rho v V)\\ &= -\frac{\partial\rho}{\partial y} + \rho f_y + (F_y)_{viscous}\frac{\partial(\rho w)}{\partial t} + \nabla \bullet (\rho w V)\\ &= -\frac{\partial\rho}{\partial z} + \rho f_z + (F_z)_{viscous}\end{aligned} \tag{8}$$

Where (f_x, f_y, f_z) and (F_x, F_y, F_z) are the x,y,z, component of the body and viscous forces respectively. u, v and w are the velocity components in the x, y, z direction respectively.

Applying the Newton's second law to and considering an infinitesimally small moving fluid element of fixed mass, the equation of momentum conservation in x, y, z directions become,

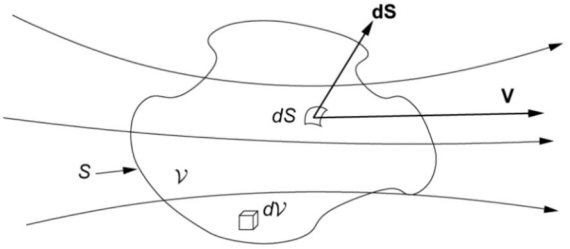


Fig. 2. Finite control volume fixed in space (Irschik & Holl, 2015).

$$\rho\frac{Du}{Dt} = -\frac{\partial\rho}{\partial x}+\frac{\partial\tau_{xx}}{\partial x}+\frac{\partial\tau_{yx}}{\partial y}+\frac{\partial\tau_{zx}}{\partial z}\rho\frac{Dv}{Dt} = -\frac{\partial\rho}{\partial y}+\frac{\partial\tau_{yy}}{\partial x}+\frac{\partial\tau_{xy}}{\partial y}+\frac{\partial\tau_{zy}}{\partial z}\rho\frac{Dw}{Dt} = -\frac{\partial\rho}{\partial z}+\frac{\partial\tau_{zz}}{\partial z}+\frac{\partial\tau_{xz}}{\partial x}+\frac{\partial\tau_{yz}}{\partial y} \quad (9)$$

for $\vec{x}$ simplified as, $\frac{\partial(\rho u)}{\partial t}+div(\rho u\vec{u}) = -\frac{\partial\rho}{\partial x}+\frac{\partial\tau_{xx}}{\partial x}+\frac{\partial\tau_{yx}}{\partial y}+\frac{\partial\tau_{zx}}{\partial z}+F_x$ (10)

To model the turbulence in the flow field, the following equations are solved numerically to determine the turbulence kinetic energy and dissipation rate for the standard k-ε model,

$$\frac{\partial(\rho k)}{\partial t}+\frac{\partial(\rho k u_j)}{\partial x_j} = \frac{\partial}{\partial x_j}\left[\left(\mu+\frac{\mu_t}{\delta_k}\right)\frac{\partial k}{\partial x_j}\right]+G_k+G_b-\rho\varepsilon-Y_M+S_k \quad (11)$$

$$\frac{\partial(\rho\varepsilon)}{\partial t}+\frac{\partial(\rho\varepsilon u_j)}{\partial x_j} = \frac{\partial}{\partial x_j}\left[\left(\mu+\frac{\mu_t}{\delta_\varepsilon}\right)\frac{\partial\varepsilon}{\partial x_j}\right]+C_{1\varepsilon}\frac{\varepsilon}{k}(G_k+C_{3\varepsilon}G_b)-C_{2\varepsilon}\rho\frac{\varepsilon^2}{k}+S_\varepsilon \quad (12)$$

The turbulence kinetic energy and dissipation rate equations evaluated in the realizable K-Epsilon model are:

$$\frac{\partial(\rho k)}{\partial t}+\frac{\partial(\rho k u_j)}{\partial x_j} = \frac{\partial}{\partial x_j}\left[\left(\mu+\frac{\mu_t}{\delta_k}\right)\frac{\partial k}{\partial x_j}\right]+G_k+G_b-\rho\varepsilon-Y_M+S_k \quad (13)$$

$$\frac{\partial(\rho\varepsilon)}{\partial t}+\frac{\partial(\rho\varepsilon u_j)}{\partial x_j} = \frac{\partial}{\partial x_j}\left[\left(\mu+\frac{\mu_t}{\delta_\varepsilon}\right)\frac{\partial\varepsilon}{\partial x_j}\right]+\rho C_1 S\varepsilon-\rho C_2\frac{\varepsilon^2}{k+\sqrt{\nu\varepsilon}}+C_{1\varepsilon}\frac{\varepsilon}{k}C_{3\varepsilon}G_b+S_\varepsilon \quad (14)$$

For the standard Low Reynolds Number K-Epsilon model (LIEN), the turbulence kinetic energy and dissipation rate equations become;

$$\frac{\partial(\rho k)}{\partial t}+\frac{\partial(\rho k u_j)}{\partial x_j} = \frac{\partial}{\partial x_j}\left[\left(\mu+\frac{\mu_t}{\delta_k}\right)\frac{\partial k}{\partial x_j}\right]+G_k+G_b-\rho\varepsilon+S_k \quad (15)$$

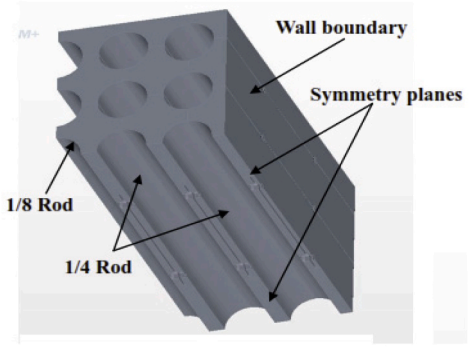
$$\frac{\partial(\rho\varepsilon)}{\partial t}+\frac{\partial(\rho\varepsilon u_j)}{\partial x_j} = \frac{\partial}{\partial x_j}\left[\left(\mu+\frac{\mu_t}{\delta_\varepsilon}\right)\frac{\partial\varepsilon}{\partial x_j}\right]+C_{1\varepsilon}f_1\frac{\varepsilon}{k}(G_k+G_b)-C_{2\varepsilon}f_2\rho\frac{\varepsilon^2}{k}+S_\varepsilon \quad (16)$$

Some studies have been carried out in analysing the effects of flow interventions. Table 1 presents some of the research conducted and a summary of their findings.

2. Methodology

In this study, the flow interventions analysed are, a square duct enclosing a 5x5 rod bundle arrangement supported by a spacer grid with split mixing vanes, swirl mixing vanes, only spacer grid and with no spacer grid. A quarter geometry of these rod bundle arrangements was sketched and designed using Computer Aided Design (CAD) tools integrated into the computational fluid dynamics code STAR-CCM + . The geometries were designed to allow for a 1 m length of the fluid domain. Figs. 3a–3c shows a quarter geometry of rod bundle, the central arrangement and the wall arrangement of the subchannel.

The meshing method in this work was carried out using a prism layer mesher to increase the accuracy of the solution at walls and boundaries, a polyhedral mesher for volume meshing, and a surface remesher for surface meshing. This was carried out using the STAR-CCM + code's continuum tool. Prior to volume meshing, the surface mesh was improved using the surface remesher. Tetrahedral and trimmed meshers

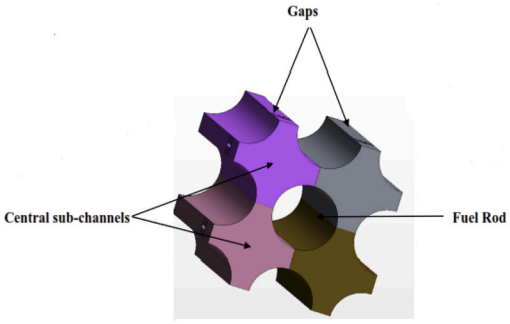


a: Quarter geometry of fuel rod bundle

Fig. 3a. Quarter geometry of fuel rod bundle.

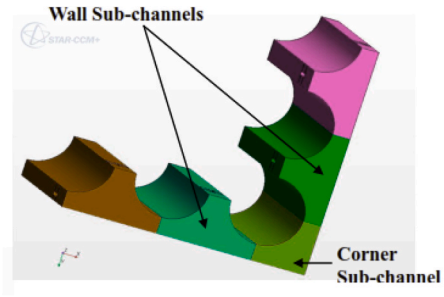
Table 1
Literature findings.

Study	Method	Reynolds Number (Re)	Flow Type	Rod Geometry	Major Findings
Lee et al. (2020)	Experimental (2D-PIV, index matching)	1.0×10^4	Single-phase (water)	5 × 5 rod bundle, square duct, 11 mm hydraulic diameter, 14 mm pitch, 4 mm spacing, 4 spacer grids (no mixing vanes)	Proposed a new mixing coefficient (lateral turbulence intensity / streamwise velocity). Found strong spatial variation in turbulence mixing across subchannels.
Qu et al. (2019)	Experimental (High fidelity 2D-PIV, MIR technique)	3.96×10^4	Single-phase (water)	5 × 5 rod bundle, PWR-type, 9.5 mm rods, 12.6 mm pitch, with mixing-vane spacer grids	Lateral flow magnitude highest in gaps, decays from 3Dh to 20Dh. Mixing vanes strongly influenced crossflow pattern and turbulence generation.
Moller (1992)	Experimental (hot-wire, pitot tube, microphones)	Turbulent regime (mean velocity ≈ 25.5 m/s, Re not explicitly stated)	Single-phase (air)	4-rod bundle in rectangular channel, aluminum rods, different P/D and W/D ratios	Determined mixing factors from turbulent fluctuations. Mixing velocity due to large eddies crossing gaps. Proposed phenomenological model for pulsations.
Shen et al. (1991)	Experimental (Laser Doppler Velocimetry, LDV)	1.42×10^4	Single-phase (water)	16-rod bundle, stainless steel rods (6 mm Ø), with and without spacer grids with mixing blades	Mixing blades created vortex flows, enhanced mixing with increasing blade angle. Large blade angles caused higher mixing but greater non-uniformity and velocity inversion.
Wang et al. (2019)	Simulation (CFD, ANSYS, MATiSH benchmark)	Not explicitly stated (benchmark PWR conditions)	Single-phase (water, PWR coolant)	5 × 5 rod bundle, advanced PWR with spacer grids and mixing vanes	Spacer grids and vanes caused local acceleration/deceleration, pressure rise, then stabilization ~ 3Dh downstream. Validated CFD's predictive capability for turbulence in subchannels.
Agbodemegbe et al. (2015, 2016)	Simulation (STAR-CCM+, polyhedral mesh, k-ε turbulence model)	Based on MATiSH (experimental Re range, single-phase water)	Single-phase (water)	5 × 5 rod bundle, square duct, spacer grids with split mixing vanes	Proposed cross-flow enhancement factor (gap width/centroid distance). Found crossflow increases with larger gaps and smaller centroid spacing. Simulation matched experiments; mixing vanes caused counter-flow and increased turbulence.



b: central subchannel arrangement

Fig. 3b. Central subchannel arrangement.



c: Wall and corner subchannel arrangement

Fig. 3c. Wall and corner subchannel arrangement.

were the alternative options that were used before the polyhedral mesher. The polyhedral mesher was applied because it is most suitable for thermodynamic simulations such as cross flow which is one of the focuses of this study. The polyhedral mesher is also relatively easy and efficient to build. It contains approximately five times fewer cells than the tetrahedral mesh for the same starting surface. Also, the polyhedral volume mesh has the fastest convergence with less iteration, the most robust convergence to lower residuals and the fastest solution runtimes as compared to the hexahedral and tetrahedral meshing.

The prism layer mesher model was used with the core volume mesh to generate orthogonal prismatic cells next to wall surfaces or boundaries. This layer of cells is necessary to improve the accuracy of the solution on the walls. The parameters that define the prism layer are the thickness, the number of cell layers in it, the size distribution of the layers and the function that is used to generate the distribution (geometric progression or hyperbolic function).

The meshing method in this work was carried out using a prism layer mesher to increase the accuracy of the solution at walls and boundaries, a polyhedral mesher for volume meshing, and a surface remesher for surface meshing. This was carried out using the STAR-CCM + code's continuum tool using the two-layer realizable k-ε turbulent flow model. Prior to volume meshing, the surface mesh was improved using the surface remesher. Tetrahedral and trimmed meshers were the alternative options that were used before the polyhedral mesher. Since thermodynamic simulations like cross flow, which are a focus of this work, are best suited for the polyhedral mesher, it was used. Additionally, building the polyhedral mesher is comparatively simple and effective. For the same starting surface, it has about five times less cells than the tetrahedral mesh. Additionally, when compared to hexahedral and tetrahedral meshing, the polyhedral volume mesh exhibits the fastest solution runtimes, the most durable convergence to reduced residuals, and the fastest convergence with less iterations.

To create orthogonal prismatic cells adjacent to wall surfaces or borders, the prism layer mesher model was combined with the core volume mesh. To increase the precision of the solution on the walls, this layer of cells is required. The thickness, number of cell layers, size distribution of the layers, and function used to generate the distribution (either a hyperbolic function or geometric progression) are the characteristics that define the prism layer.

In this study, the mesh sensitivity was carried out by varying the base sizes as shown in Table 2. The base sizes used are 1 mm, 5 mm and 10 mm. Figs. 4 to 7 presents the geometries after meshing.

To model the turbulent flow, the two-layer realizable k-ε model was used. This was selected after a turbulence model sensitivity study was performed. The results of the sensitivity analysis are presented in this work. The turbulence kinetic energy and dissipation rate equations to be solved in the two-layer realizable k-ε model are as described in equations (11)–(14).

A wall treatment in STAR-CCM + is the set of near-wall modelling assumptions for each turbulence model. The wall treatments have been specialized according to each turbulence model, since assumptions specific to that model must be made for the wall boundary conditions for the turbulence quantities. The three types of wall treatment provided in STAR-CCM + include high-y^+, low-y^+ and all-y^+ wall treatments (Cd-Adapco, 2015). The physics models and reference values employed in this study are presented in Tables 4 and 5.

In fluid mechanics, especially in boundary layer theory and turbulence modeling y + is a dimensionless wall distance that tells how far a point is from a wall in terms of viscous scaling. It is generally determined as,

$$y+ = yu_\tau/\nu \tag{17}$$

where "y" is the distance (m) from the wall, ν is the kinematic viscosity and u_τ is the friction velocity defined as,

$$u_\tau = \sqrt{(\tau_w/\rho)} \tag{18}$$

where τ_w is the wall shear stress and ρ is the fluid density.

Typical targets of y + for low Reynolds number (ie $y+ \approx 1$) resolves boundary layer and wall functions employ high Reynolds models ($30 < y+ < 300$). Suitable ranges for y + for turbulence models are presented in Table 3.

In the present work, after determining the Reynolds number ($Re = GD/\mu$), the skin friction coefficient by virtue of Blasius correlation ($C_f = 0.079/Re^{0.25}$) was determined for turbulent flow, the wall shear stress $\tau_w = ½(\rho u^2 C_f)$ and the friction velocity $u_\tau = \sqrt{(\tau_w/\rho)}$ were computed. The first prism layer thickness of 1.0×10^{-3} with a growth rate of 1.4 was set leading to the distribution of wall y + extracted across the domain in the range of $y+ \leq 35$ as presented in Fig. 8.

The wall y + range obtained dictates the ability to resolve turbulence within the viscous sublayer and beyond the transition zone between viscous sub-layer and log law regions ($1 < y+ < 30$). Near wall turbulence is predicted with higher accuracy using the two-layer turbulence models. With an all y + wall treatment, the present approach appropriately blends wall treatment that works across all y + range, automatically transitioning between the viscous sub-layer formulation (low y +) and the log law wall function (high y +). This works in such a way that when $y+ > 30$, further from the wall, the approach employs wall functions. When $y+ \leq 1$, near wall treatment is employed. The transition wall treatment resolves viscous effect and implements smooth interpolation in the intermediate region of $1 < y+ < 30$.

Table 2
Comparison of Mesh Sizes.

Mesh variation	Base Size	No. of cells
M1	1 mm	3,386,257
M2	5 mm	1,508,592
M3	10 mm	864,606

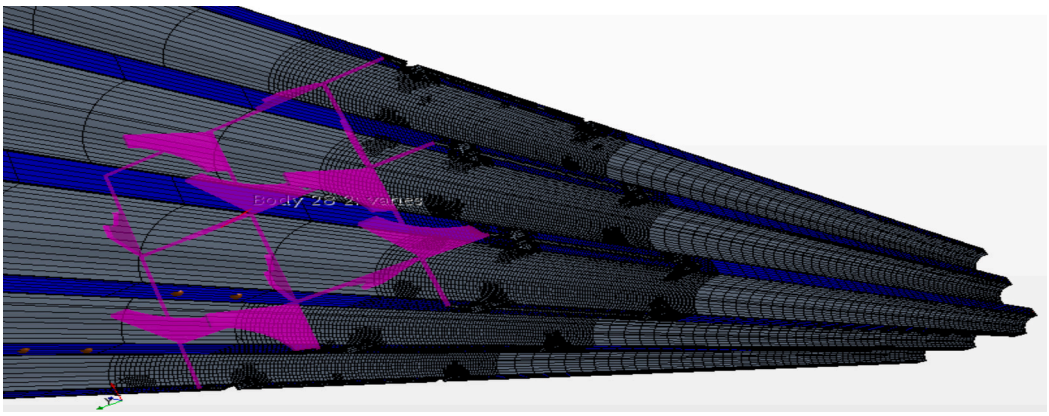


Fig. 4. Quarter geometry of spacer grid with split vane after meshing.

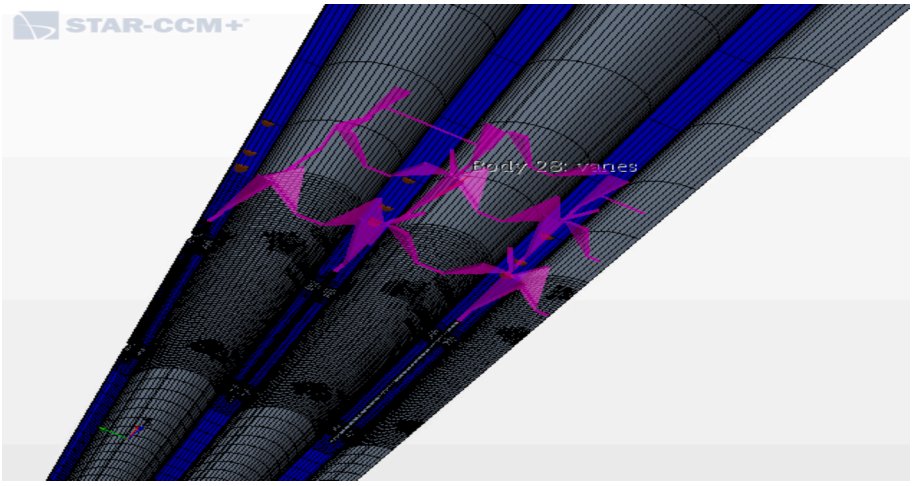


Fig. 5. Quarter geometry of spacer grid with swirl vane after meshing.

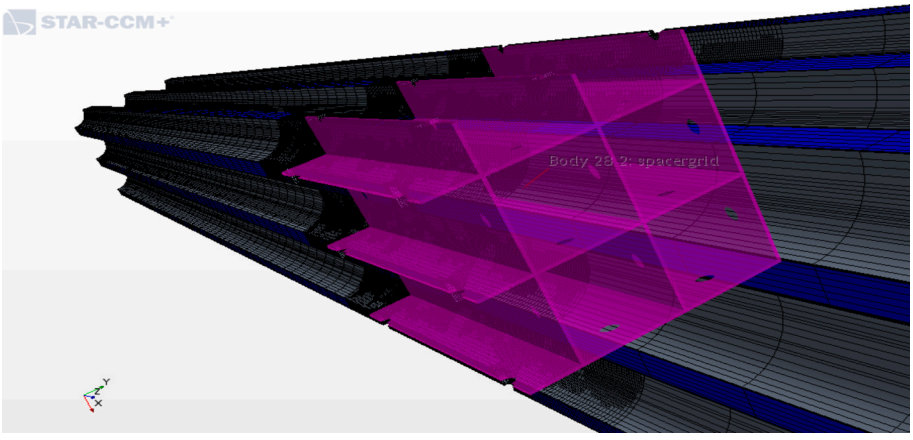


Fig. 6. Quarter geometry of fuel bundle with spacer grid after meshing.

The numerical results were verified using the convergence plot of the flow variables. The convergence plot displays the alteration of the flow variables as the solver iterates. For a steady state flow, the gradient of these variables becomes zero. To validate the results, the numerical results will be compared to experimental data from the Organization for Economic Co-operation and Development/Nuclear Energy Agency – Korea Atomic Energy Research Institute, Measurement and Analysis of Turbulent Mixing In Sub- Channels – Horizontal (OECD/NEA-KAERI MATiS-H) test facility. The OECD/NEA-KAERI MATiS-H Benchmark was initiated to test the ability of state-of-the-art. Computational Fluid Dynamics (CFD) codes to predict important turbulence parameters downstream of a generic design of spacer grid in a rod-bundle geometry. The Measurements and Analysis of Turbulence in Subchannels-Horizontal (MATiS-H) experimental facility at the Korea Atomic Energy Research Institute (KAERI) has been used in the past in the development of advanced nuclear fuels in Korea. The test section consists of a square

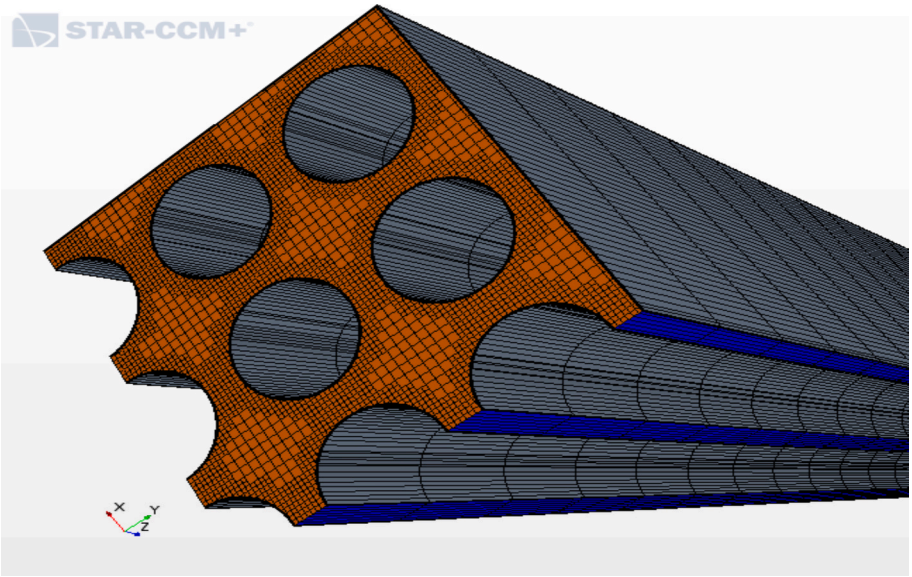


Fig. 7. Quarter geometry of fuel bundle without spacer grid after meshing.

Table 3
Suitable y + Ranges for Turbulence Models.

Turbulence Model	Near-Wall Treatment	Recommended y + Range	Notes
Standard k-ε	Wall functions	$30 \leq y+ \leq 300$	Cannot resolve viscous sublayer directly.
Realizable k-ε (with wall functions)	Wall functions	$30 \leq y+ \leq 300$	Similar to standard, but with improved stress formulation.
Two-layer realizable k-ε	Two-layer approach (viscous + log-law)	$y+ < 1$	Resolves viscous sublayer explicitly; mesh must be fine near the wall.
RNG k-ε	Enhanced wall treatment	$y+ \approx 1$ or 30–300 depending on setup	More flexible than standard.
SST k-ω	Low-Re treatment	$y+ < 1$	Designed for accurate near-wall resolution.

Table 4
Physics Models used in the Simulation.

Physics Models	
Model	**Model Specification**
Space model	3-Dimensional
Time model	Implicit unsteady
Material model	Liquid (water in single phase)
Equation of state model	Constant density
Flow model	Segregated flow
Energy model	Segregated fluid isothermal
Viscous regime model	Turbulent
Turbulence model	k-epsilon
k-epsilon model	Realizable two −layer
Wall treatment	All y+
Convection Scheme	Second Order upwind

Table 5
Reference values used in Modelling.

Prism Layer mesh reference values	
Parameter	**Value**
Number of prism layers	4
Prism layer stretching	Geometric progression
Absolute size	0.002 *m*

channel of 170x170 mm cross-section and 4670 mm length. The channel contains a 5x5 rod bundle, each of the 25 rods being of 25.4 mm outer diameter and 3863 mm in length, representing the fuel rods in an actual fuel bundle. The numerical data presented in this study are average data taken at various respective regions of the flow domain.

3. Results and discussion

3.1. Mesh sensitivity

In this study, the meshes shown in Table 2 were obtained by varying the base sizes (1 mm, 5 mm, 10 mm). Fig. 9 presents the graphical representation of the transverse velocities for the varied meshes with the experimental data. In the graph M1, M2, M3 represents meshing with base sizes 1 mm, 5 mm and 10 mm respectively, Exp. represents experimental results.

As observed in Fig. 9, the meshes with base sizes of 1 mm and 5 mm show good agreement with the experimental data. Mesh model with base size of 10 mm generally has curves similar to that of the experimental data but do not quantitatively show similar or close peaks and troughs. Considering the computational resources and time required to run all the numerical simulations using mesh with base size 1 mm and the fact that they produced very similar agreement with the experimental data, mesh model with base size 5 mm was selected for all the simulations in this study.

3.2. Turbulence model sensitivity

The sensitivity of the turbulence models is presented in Fig. 9. In the graph, std. k-ε represents result obtained using the turbulence model standard k epsilon, K- ω represents k-omega, 2lyr. R. k-ε represents two-layer realizable k-epsilon and Exp. represents experimental results. It was observed that the models showed similar distribution trends. The difference in peak values could be as a result of the in-code approximations and wall treatment effects specific to the model.

Though all the three (3) turbulence models, standard k-ε model (std. k-ε), k-omega (K- ω) and the two-layer realizable k-ε model (2lyr. R. k-ε) compared closely predicted the experimental data in Fig. 9 and standard k-ε model (std. k-ε) appeared to show slightly better prediction, the two-layer realizable k-ε model was selected for numerical simulations. Because the two-layer realizable k-ε model was used for similar numerical studies (Agbodemegbe et al., 2015 and 2016), and also being

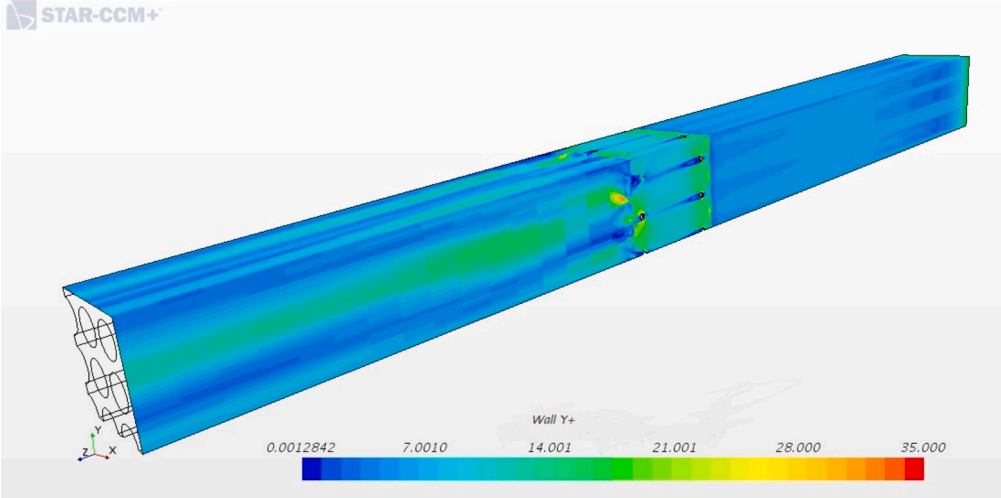


Fig. 8. Wall y + Distribution Scene.

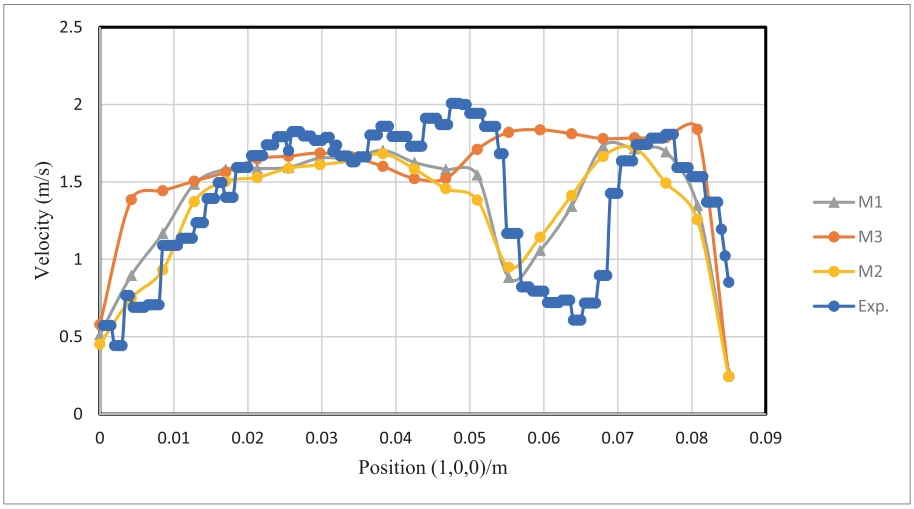


Fig. 9. Comparison of transverse velocity for different turbulent models with experimental data.

guided by literature information provided in Table 3. The two-layer realizable k-ε model produced good results in these studies.

For the verification of the model, a test for convergence was performed. In this study, flow simulation convergence was attained mainly within the range of 2000—2600 iteration steps. Convergence of the solution was judged via residual plots and monitors. The default setting of the normalized residuals ie. continuity, momentum, energy and turbulence were kept at residual drop by 3 orders of magnitude (ie. 10^{-3}).

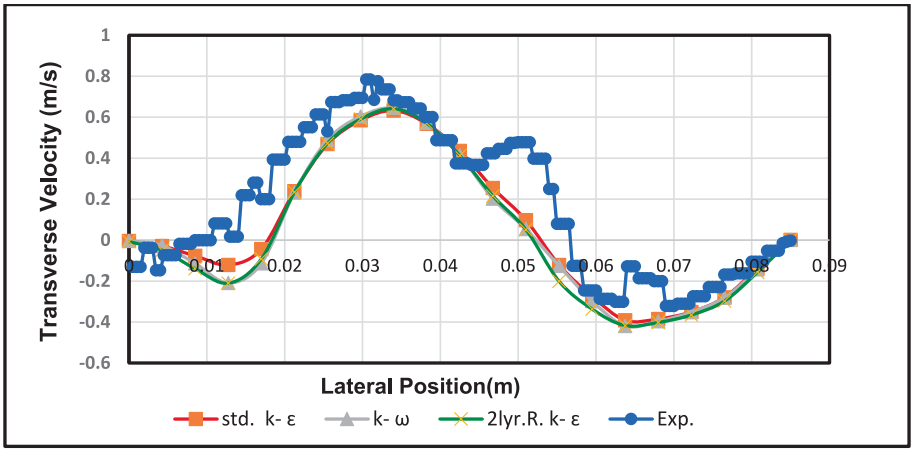


Fig. 10. Comparison of transverse velocity of different mesh sizes with experimental data.

Monitor plot of axial velocity at exit of the domain was also relied on to support and confirm the convergence of flow parameter. The axial velocity monitor plot placed at the flow exit to monitor convergence is shown in Fig. 10.

3.3. Model validation

The extent of predictability of the split vane effect by CFD was determined by comparing trends of the experimental data with the simulation results. Data was compared over line probe located at the lateral position Y1 and axial position of 1.0 hydraulic diameter (1.0 Dh) and downstream 10.0Dh. Fig. 11 shows the positions for data extraction in the geometry.

Figs. 12 and 13 show the comparison axial and transverse flow velocity evaluated from the simulation to that of the experimental results for the case of spacer grid with split vane.

A comparison of the simulation data for the axial velocity distribution and the experimental data is presented in Fig. 12. A good agreement of the simulation data with the experimental data are evident with higher extents of crossflow predicted in the gap regions for the simulation results than for the experimental data. The graph of transverse velocity for the simulation data compared with the experimental data is also shown in Fig. 13. The graph from the simulation data compared well with the experimental data, although some level of deviations of the simulation data from the experimental are observed, this can be attributed to some approximations inherent in the CFD code. The trend of the experimental data is quite well predicted and most of the numerical results are within the acceptable limit of $\pm$ 10% compared to the experimental data. Similar agreement was also realized in the investigation performed by (Lee et al., 2020; Agbodemegbe et al., 2016, Pacio et al., 2015; Podila et al., 2014).

3.4. Turbulence

Having validated the model used for the study, parameters that indicate turbulence, crossflow and mixing are compared for the quarter geometries with and without structural interventions. The turbulent kinetic energy (TKE) and turbulent dissipation rate (ε) plots provide vital information on the turbulence production and decay characteristics induced by various spacer designs at 1.0DhU.

The TKE graph in Fig. 14 clearly demonstrates that the spacer grid with swirl vane configurations produce the highest turbulence levels, with peak values exceeding 1.4 m^2/s^2. This indicates intense turbulence generation, likely driven by flow separation and recirculation zones initiated by these spacers. The split vane follows with moderate energy levels, while the no-spacer case remains nearly flat and minimal, confirming negligible turbulence in the absence of mechanical flow disruptions. In CFD models such as the RANS-based k−∈ model, the turbulent viscosity is directly dependent on the ratio $V_t = C_\mu \frac{k^2}{\in}$, where k is the TKE and ∈ is the dissipation rate (Zhu et al., 2014).

The plot of turbulent dissipation rate in Fig. 15 further supports the observed trend, with the split vane exhibiting the highest ε values, especially beyond 0.05 m along the flow direction. This indicates rapid conversion of turbulent energy into thermal energy via viscous effects, a sign of fully developed turbulent regions. The swirl vane also maintains consistently high dissipation across the domain, showing its effectiveness in sustaining turbulent flow downstream. The spacer grid exhibits multiple ε peaks, which may correspond to localized eddy shedding or reattachment zones typical in bluff-body flows. The no-spacer configuration again shows minimal dissipation, aligning with its low TKE.

3.5. Vorticity

The tendency of the fluid or coolant to form swirls represents its vorticity. The study observed the variation in the axial vorticity, transverse vorticity and spanwise vorticity for the rod bundles. Figs. 16–18 presents graphical representation of the findings.

The axial vorticity plot in Fig. 16 reveals significant differences in vortex dynamics across the various spacer configurations. The swirl vane configuration induces the strongest axial vorticity oscillations, with values ranging from approximately −250 s^{-1} to over 250 s^{-1}, indicating intense rotational flow along the axial direction. This is consistent with the swirl vane's purpose of generating helical flow structures. The split vane also shows substantial axial vorticity, although the amplitude is slightly lower, suggesting a more moderated rotational field. In contrast, the spacer grid produces relatively minor axial vorticity, mostly centred around zero, while the no-spacer condition exhibits negligible vorticity throughout the measurement domain. These observations underscore that spacer grid with mixing vane configurations are highly effective at generating axial vortices, which can enhance turbulence mixing and heat transfer (Li et al., 2019).

In the spanwise vorticity plot, Fig. 17, distinct trends emerge. The no-spacer condition uniquely exhibits consistent positive vorticity values around 80–100 s^{-1}, which may be attributed to residual boundary layer effects or natural flow stratification. In contrast, the other configurations, especially the spacer grid and split vane, show dominant negative vorticity values, reaching nearly −300 s^{-1}. The periodic patterns for the spacer grid with mixing vane configurations indicate a strong induced secondary flow that alternates across the domain, likely due to flow separation and reattachment triggered by vane structures. The swirl vane configuration shows less extreme spanwise vorticity than the spacer grid, suggesting a more balanced but still effective flow manipulation. These findings align with prior research noting that structured spacers lead to complex secondary flow patterns that strongly affect

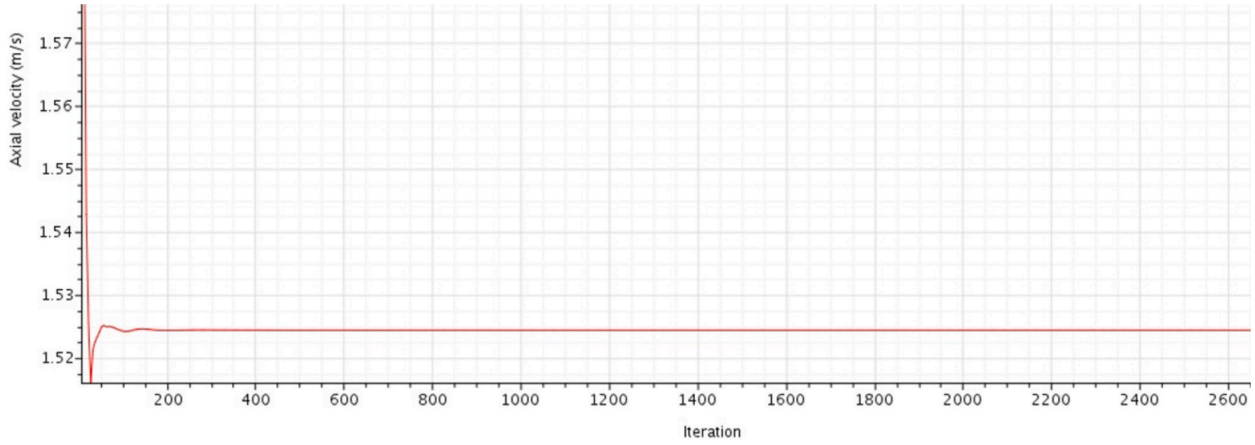


Fig. 11. Graph of axial velocity against number of iterations for Split vane geometry.

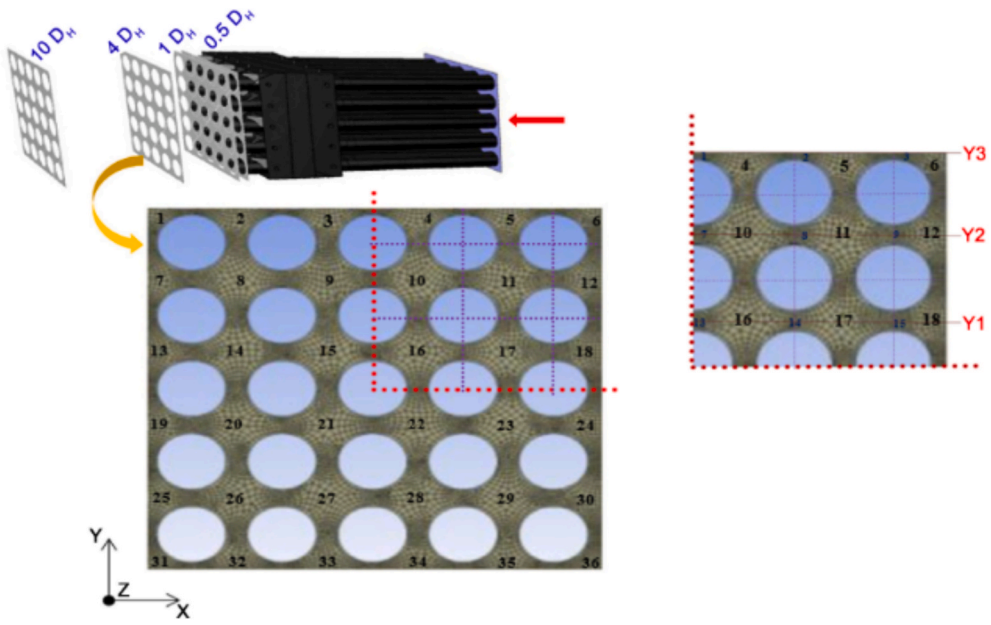


Fig. 12. Data extraction positions in Fuel bundle geometries.

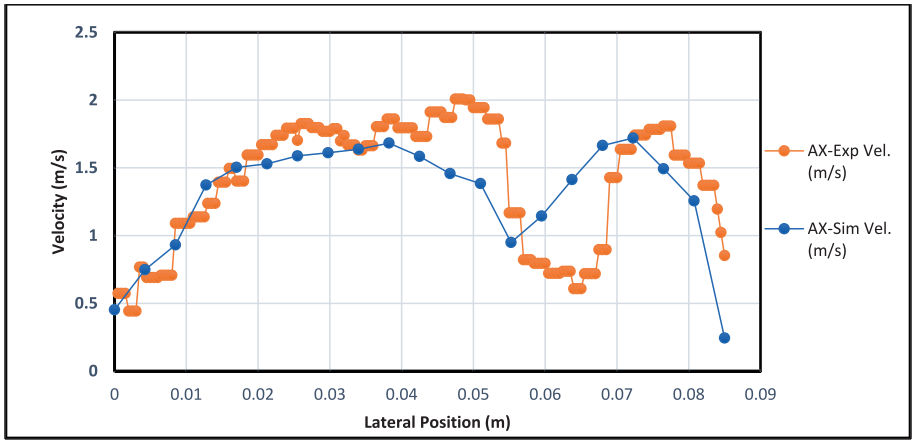


Fig. 13. Graph of Axial velocity for Simulation and Experimental results.

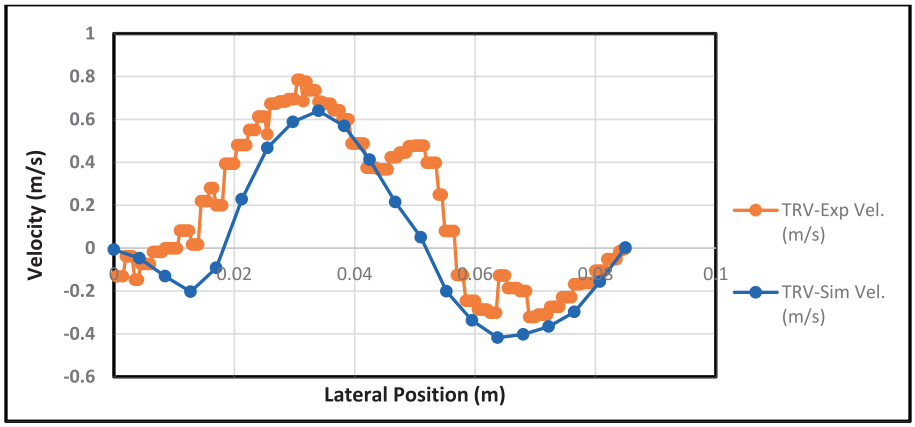


Fig. 14. Graph of transverse velocity for Simulation and Experimental results.

lateral fluid transport (Park et al., 2020).

The transverse vorticity plot presented in Fig. 18 further emphasizes the role of vane geometry in shaping flow fields. The swirl vane again produces the highest peaks, exceeding 100 s^{-1}, with rapid oscillations indicating the development of strong cross-stream vortices. The split vane and spacer grid configurations follow, with moderate but clearly

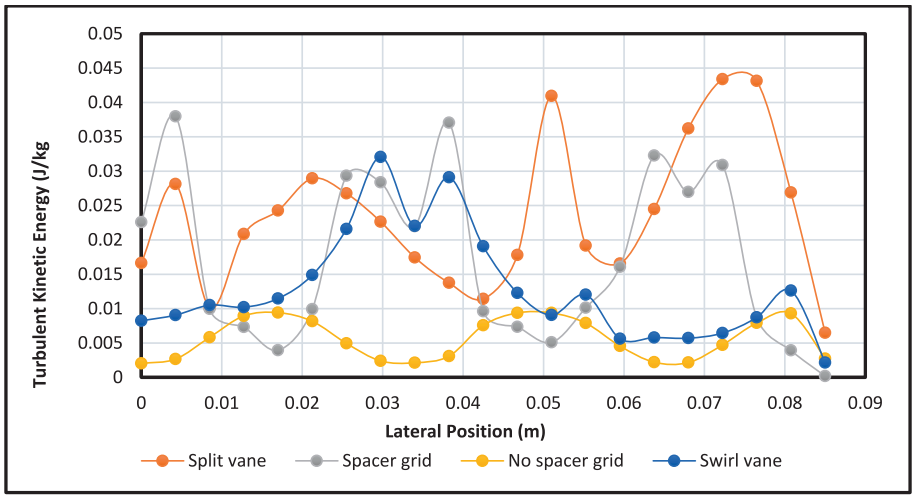


Fig. 15. Graph of turbulent kinetic energy for rod bundle geometries at 1.0Dh downstream.

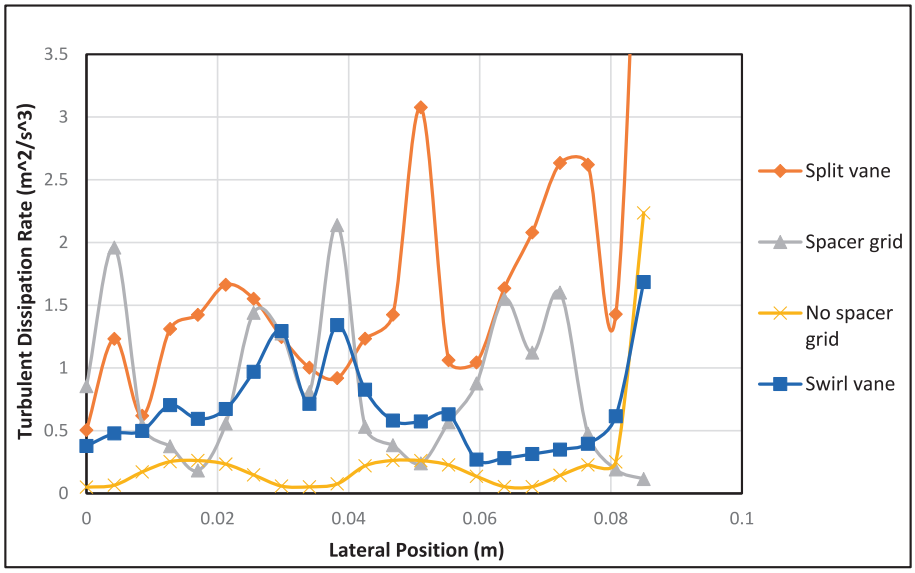


Fig. 16. Graph of turbulent dissipation rate for rod bundle geometries at 1.0Dh downstream.

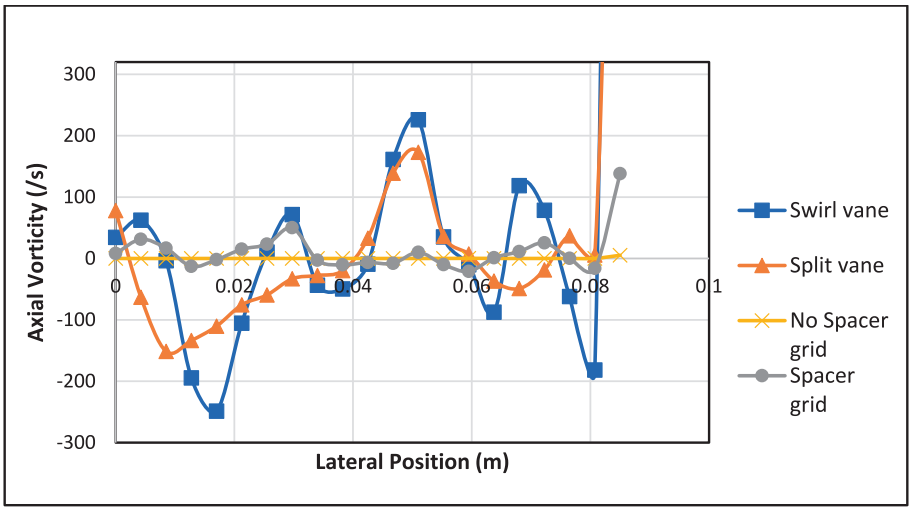


Fig. 17. Graph of axial vorticity for rod bundle geometries at 1.0Dh.

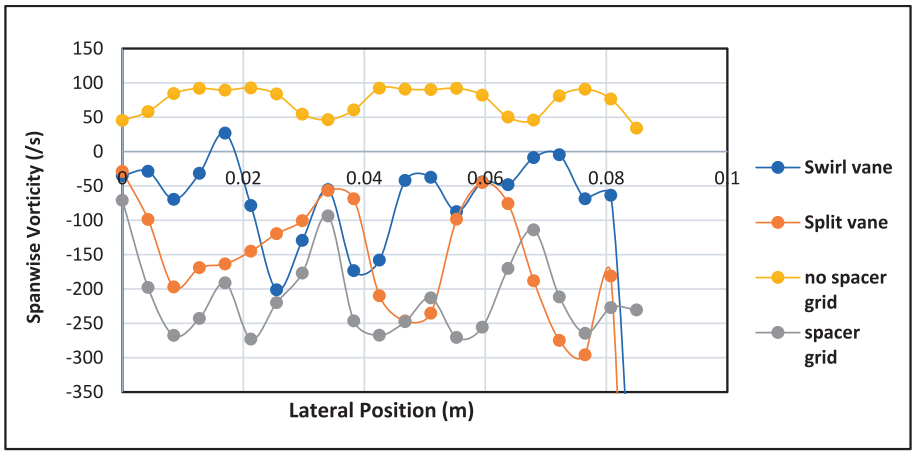


Fig. 18. Graph of spanwise vorticity for rod bundle geometries at 1.0Dh.

structured fluctuations. In contrast, the no-spacer grid remains near zero, consistent with minimal disruption to the baseline flow. The presence of alternating peaks and troughs in the spacer grid with mixing vane configurations indicates coherent vortex shedding or wake interactions, which are known to improve mixing and reduce stagnation. The data suggest that the swirl vane not only influences axial flow but also contributes strongly to transverse and lateral vortex structures, confirming its multidimensional impact on turbulence intensification (Ren et al., 2018).

3.6. Velocity

The velocity magnitude, axial velocity, transverse velocity and spanwise velocity for the rod bundle quarter geometries are presented and discussed.

Fig. 19 presents the velocity magnitude distribution along the lateral direction [1,0,0] at a downstream location of 1.0 Hydraulic Diameter (Dh) for four different rod bundle geometries. The split vane geometry exhibits the highest peak velocities, reaching values up to 2.0 m/s, with a relatively smooth and symmetric profile. This behaviour suggests a strong acceleration of the flow due to effective channelling and redirection of fluid by the vane structures, as supported by previous studies highlighting the enhanced axial momentum imparted by split vanes (Matozinhos et al., 2021). The swirl vane geometry shows moderate velocity fluctuations around 1.2 m/s, characterized by periodic peaks and troughs—indicating a strong influence of swirling-induced cross-flow redistribution. The no spacer grid case maintains a nearly uniform velocity profile with minor undulations, indicating undisturbed flow but limited enhancement of mixing or momentum transfer. In contrast, the conventional spacer grid (without vanes) shows the lowest average velocity magnitude and most pronounced periodic dips, implying significant flow obstruction with less effective mixing. These findings reinforce that vane-type spacers not only increase flow turbulence but also enhance axial flow uniformity, which is crucial for optimizing heat transfer and minimizing localized hotspots in nuclear fuel assemblies (Lee et al., 2014). The comparative performance illustrates the importance of structural design in shaping thermal–hydraulic behaviour within rod bundles.

Fig. 20 illustrates the overall velocity distribution at a downstream location of 10 hydraulic diameters (10.0Dh) for various spacer grid configurations within a nuclear rod bundle. The data show that the split vane spacer grid maintains the highest lateral velocity magnitude across most of the domain, exceeding 1.7 m/s, indicating a sustained axial momentum induced by the vane geometry. This aligns with prior findings that vane-type grids, especially split vanes, effectively channel flow and suppress recirculation, thereby enhancing crossflow and axial flow penetration (Wang et al., 2021). The swirl vane configuration demonstrates periodic fluctuations with peak velocities near 1.3 m/s, suggesting that the induced tangential flow gradually weakens downstream but continues to influence axial flow distribution. The no spacer grid case yields a relatively uniform profile around 1.0 m/s, showing that while it avoids flow obstruction, it lacks enhanced flow redistribution. Conversely, the conventional spacer grid exhibits the lowest velocity magnitude (~0.7 m/s) and the most subdued axial development,

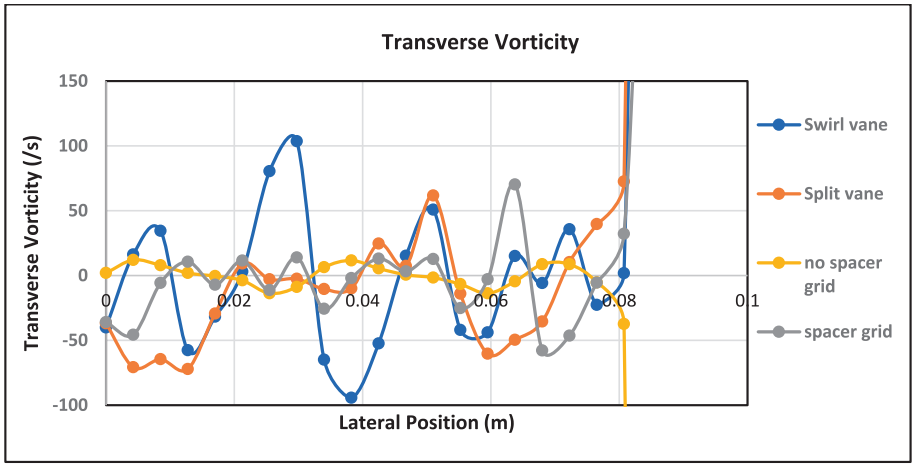


Fig. 19. Graph of transverse vorticity for rod bundle geometries at 1.0Dh.

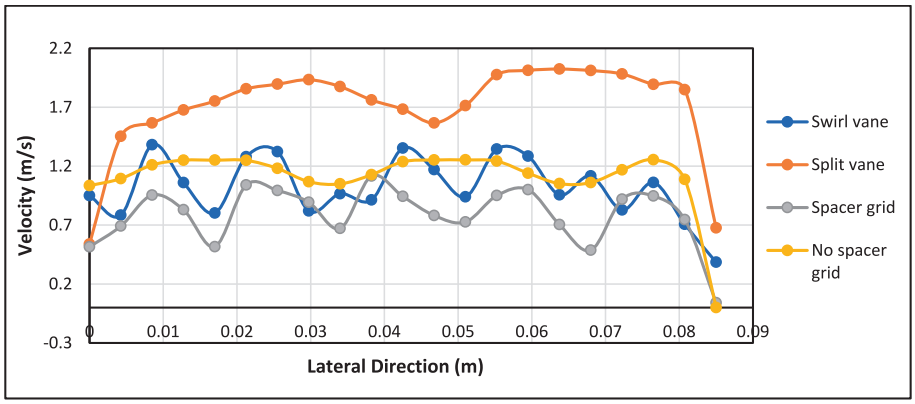


Fig. 20. Graph of magnitude of velocity for rod bundle geometries at 1.0 Dh.

implying considerable flow resistance with limited contribution to momentum enhancement. These trends confirm that structural modifications like split and swirl vanes are crucial not only for mixing enhancement but also for maintaining velocity uniformity and suppressing hotspots and non-uniform flow mixing downstream. These are essential parameters for improving heat transfer and minimizing hotspots in reactor cores (Liu et al., 2020; Moorthi et al., 2018; Ren et al., 2018).

The axial velocity distribution along the flow direction [1,0,0] for different spacer grid configurations—namely, no spacer grid, swirl vane, split vane, and spacer grid—is illustrated in Fig. 21. The data reveals significant variation in flow behaviour induced by each configuration. The split vane spacer grid shows the highest axial velocity peaks, reaching values above 1.8 m/s, indicating enhanced flow acceleration and turbulence mixing effects downstream of the vane structures. This behaviour aligns with findings in literature where split-type vanes are shown to induce strong secondary flows and higher turbulence intensities (Matozinhos et al., 2021; Qu et al., 2023). In contrast, the no spacer grid configuration maintains a negative axial velocity profile throughout, suggesting potential recirculation or reversed flow regions, a characteristic typical in undisturbed or under-developed flows (Mao et al., 2017). The Swirl vane shows moderate enhancement in axial velocity, with oscillatory behaviour likely due to swirl-induced mixing, while the standard Spacer grid produces the least velocity enhancement, staying below 0.7 m/s throughout the section. This comparative analysis reinforces the importance of vane geometry and presence in influencing coolant flow dynamics, which are critical to heat transfer efficiency and flow stability in nuclear reactor subchannels.

Fig. 22 presents the transverse velocity distribution along the [1,0,0] direction at 1.0Dh downstream of the spacer grid, highlighting the impact of various grid configurations on cross-flow behaviour. Among the quarter rod geometries analysed; swirl vane, split vane, spacer grid, and no spacer grid, the swirl vane exhibits the most significant transverse velocity oscillations, reaching peak values of approximately ± 0.12 m/s. This is indicative of the strong secondary flow structures induced by the swirling motion, which enhances lateral mixing within the subchannel. Such performance is substantiated by studies that emphasize the swirl vane's effectiveness in improving heat transfer via transverse momentum exchange and crossflow (Chang et al., 2014). The split vane also induces substantial transverse velocities, though less intense than the swirl vane, suggesting a compromise between mixing and pressure drop. In contrast, the conventional spacer grid and no spacer grid configurations demonstrate minimal cross-flow activity, with velocities near zero, indicating limited mixing potential (Lee et al., 2014). These observations support the conclusion that vane geometry plays a critical role in defining secondary flow intensity, which is essential for thermal–hydraulic performance in nuclear reactor fuel assemblies.

The spanwise velocity distribution at 1.0Dh downstream of various spacer grid configurations—swirl vane, split vane, spacer grid, and no spacer grid—along the [1,0,0] direction is presented in Fig. 23. The swirl vane and split vane configurations exhibit pronounced oscillatory behaviour in the spanwise direction, with peak velocities approaching ± 0.6 m/s and ± 0.5 m/s, respectively. This highlights their ability to induce strong lateral mixing and cross-channel flow, enhancing turbulent transport across subchannels. The split vane's symmetrical wave

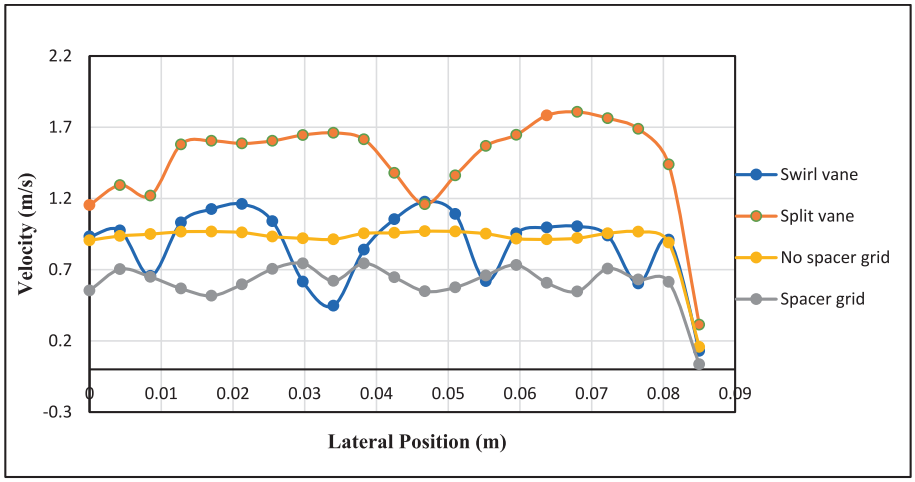


Fig. 21. Graph of magnitude of velocity for rod bundle geometries at 10.0Dh.

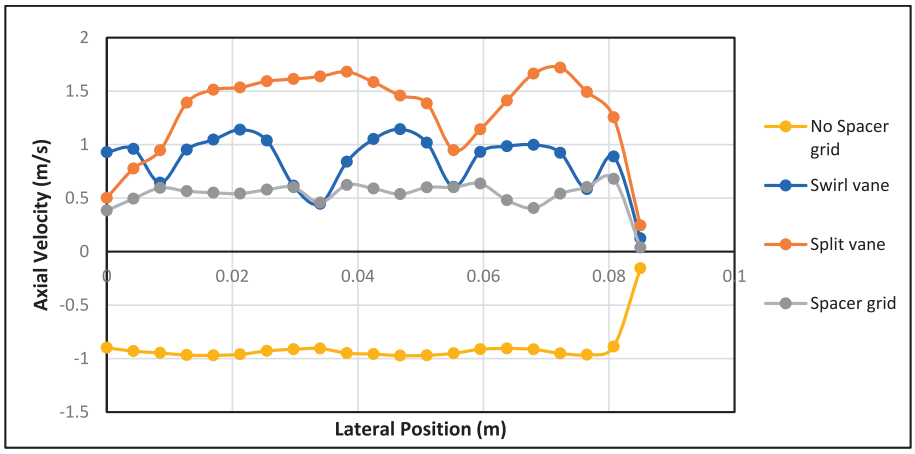


Fig. 22. Graph of axial velocity for rod bundle geometries.

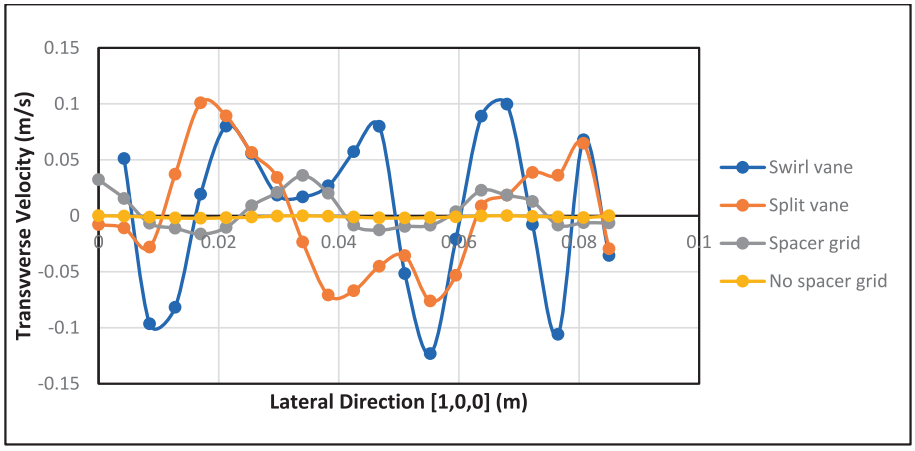


Fig. 23. Graph of transverse velocity for quarter rod geometries.

pattern is consistent with findings in computational and experimental studies that associate such designs with coherent secondary flow structures and vortex generation (Liu et al., 2020). These oscillations are a result of strong secondary flows generated by vane-induced vortex structures, which contribute to enhanced fluid mixing and redistribution of momentum across subchannels. Similar behaviours were observed by (Wang et al., 2020), who reported that mixing vanes introduce coherent vortices that promote three-dimensional flow complexity and improved thermal performance. In contrast, the conventional spacer grid and no spacer grid configurations show near-zero spanwise velocities throughout the channel, suggesting minimal disturbance to the bulk axial flow. These results reaffirm that vane-equipped grids are essential for promoting effective lateral momentum exchange, crucial for enhancing coolant mixing and heat transfer performance in reactor

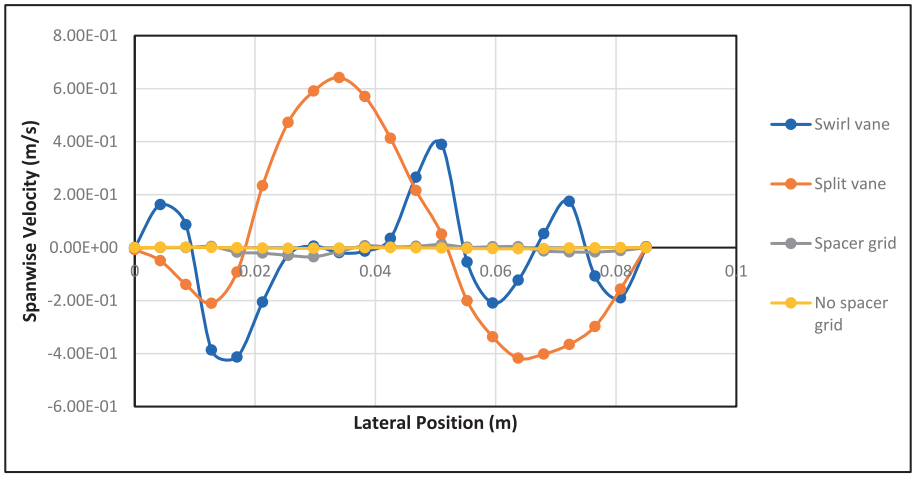


Fig. 24. Graph of spanwise velocity for quarter rod geometries at 1.0Dh.

cores (Zhang et al., 2023). Therefore, the introduction of geometrical modifications such as vanes significantly alters the three-dimensional flow field, especially in the transverse and spanwise planes. This enhanced flow mixing and heat transfer performance supports ongoing design trends favouring vane-equipped spacer grids for improved thermal–hydraulic efficiency. Table 5 presents a comparative analysis of all four geometries.

The graph of pressure drop comparison for the geometries studied in this work is presented in Fig. 24. Furthermore, a graph of pressure drop for split vane and swirl vane is presented in Fig. 25. It can be observed from the graph that the pressure drop in the fuel bundle with swirl vane is higher than in split vane cases, confirming the lower obstruction and drag forces associated with split vane geometry. This reduction in hydraulic penalty highlights split vanes as a compromise between efficient mixing and manageable pumping requirements. Although mixing performance may not match that of swirl vanes, the reduced energy costs make split vanes particularly suitable for reactors requiring operational efficiency alongside enhanced safety margins.

In the case of the swirl vane, increased drag from vane obstructions leads to higher pressure losses. Despite this drawback, the thermal–hydraulic benefits in terms of mixing and uniform heat transfer justify the pressure drops in reactor safety considerations. Optimization of vane geometry remains essential to balance improved turbulence generation against pressure losses.

3.7. Single phase turbulent mixing coefficient

In this section, results of single phase turbulent mixing coefficient are presented for the cases of the quarter rod bundle geometries. Mathematically, the axial flow velocity is related to the mixing coefficient as presented in equation (19) (Podila et al., 2014);

$$\frac{|\vec{v}|}{\beta^*} = \left[\frac{\Delta y\sqrt{\frac{2}{3\pi}}}{C_\mu}\right]\frac{\varepsilon\overline{\mu}}{k^2}\sqrt{k} = C\frac{\varepsilon\overline{\mu}}{k^2}\sqrt{k} \tag{19}$$

Assuming a characteristic velocity $\overline{U}$ defined as the square root of the turbulent kinetic energy equation (19) becomes,

$$\frac{|\vec{v}|}{\beta^*} = C\frac{\varepsilon\overline{\mu}\sqrt{k}}{k^2}\sqrt{k} = C\frac{\varepsilon}{k} \tag{20}$$

Further simplification gives the correlation between the mixing coefficient and the axial velocity fluctuation as;

$$\frac{|\vec{v}|}{\beta^*} \propto \frac{\varepsilon}{k} \tag{21}$$

Where $\vec{v}$ is the axial velocity fluctuation, turbulent k is the kinetic energy,β^* is the mixing coefficient, ε is the turbulent dissipation rate.

Equation (21) shows that the two measures of turbulent mixing are equal only under the condition that production of turbulent kinetic energy balances the rate at which it dissipates.

The results for the overall mixing effect of the rod bundle geometries across the gaps 1–3, from Fig. 26, is quantified using equation (21) and the overall mixing effect is evaluated and presented in Table 6.

The results in Table 7 provide a quantitative comparison of the single-phase turbulent mixing coefficient across different quarter rod bundle geometries. Without spacer grids, the mixing coefficients are largely negative for gaps 1 and 2, with values of –0.98 and –1.68 respectively, indicating suppressed mixing or non-uniform distribution of coolant flow in these regions. Only gap 3 shows a positive coefficient 0.67, suggesting limited natural mixing. The introduction of a spacer grid improves the overall mixing effect. This demonstrates that the grid structure alone mitigates some flow non-uniformities by enhancing lateral transport across subchannels.

When advanced spacer grid designs with split vanes or swirl vanes are incorporated, the mixing coefficients increase markedly, with values consistently above 2.0 across all gaps. The split vane spacer grid yields the highest overall mixing effect (3.43), followed closely by the swirl vane design (2.56). This result highlights the role of vane-induced secondary flows in promoting crossflow and turbulence-driven mixing, thereby improving coolant redistribution in the rod bundle. Such enhanced mixing is crucial for maintaining uniform temperature profiles, reducing hot spots, and ensuring safety margins in nuclear reactor cores. The data underscores the importance of spacer grid design optimization in reactor thermal-hydraulics, as vane geometries provide significant benefits over bare or simple grid configurations in promoting subchannel mixing.

4. Conclusion

This study analysed the mechanisms governing turbulence-induced crossflow and coolant mixing within rod bundle geometries subjected to various flow interventions, with emphasis on split vane, swirl vane, and only spacer grid and no spacer grid designs. The combined evaluation of mean flow behaviour, secondary flow structures, and turbulence characteristics revealed that vane-type spacers substantially modify momentum exchange and enhance cross-subchannel transport relative

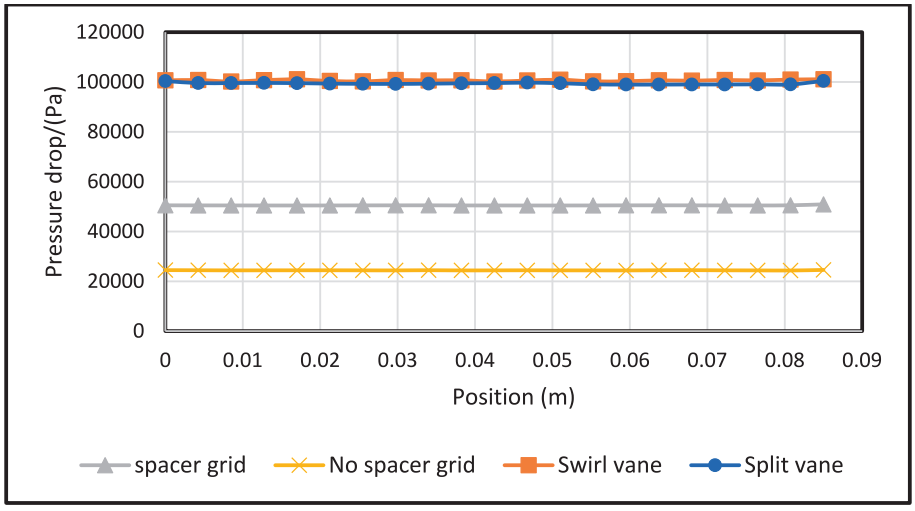


Fig. 25. Graph of Pressure drop for rod geometries.

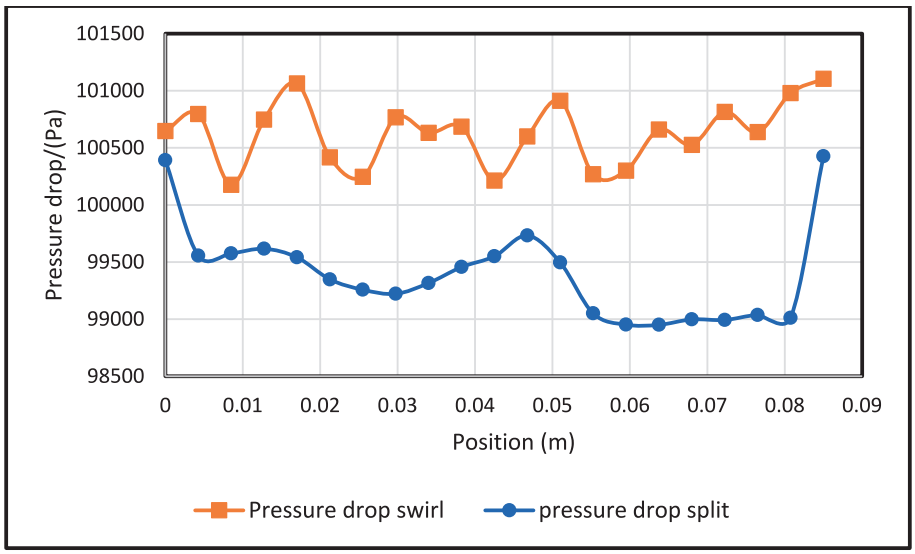


Fig. 26. Graph of Pressure drop for rod geometries with split vane and swirl vane.

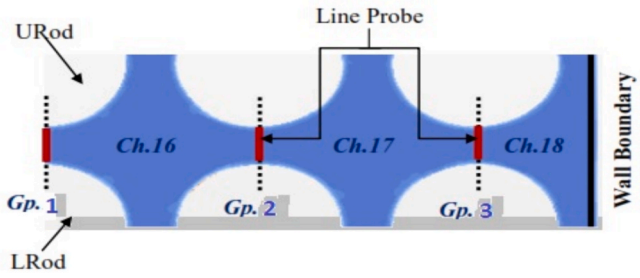


Fig. 27. Line probe positioning in gaps.

to no-spacer configurations. The turbulence metrics reinforced these observations by capturing the energy pathways within the flow. Both split vane and swirl vane designs exhibited elevated turbulent kinetic energy and dissipation rates, with swirl vanes particularly effective in sustaining dissipation downstream. The results confirmed that rod bundle geometries with mixing vanes introduce high eddy viscosity zones, facilitating enhanced scalar transport and cross-mixing across subchannels. The no-spacer condition consistently produced minimal turbulence levels, confirming its limited capacity to redistribute energy or momentum. These findings illustrate how vane-induced turbulence strengthens convective transport processes vital for efficient heat removal.

Overall, the results establish a clear link between spacer-induced crossflows, turbulence augmentation, and improved mixing performance. Swirl vanes delivered the most persistent downstream effects, while split vanes and cruciform inserts provided targeted enhancements at specific axial locations. These insights support the development of refined crossflow correlations for advanced spacer geometries and highlight the importance of turbulence-energy redistribution in optimizing thermal–hydraulic performance for next-generation reactor designs.

From the present results and analysis performed, the findings show better mixing performance and hence heat removal efficiency in rod bundles in the presence of spacer grids with mixing vanes, although at considerable pressure drops. Next generation intervention in flow mixing using these interventions should emphasise on the need to adopt higher mixed-coefficient split blades for better performance or more uniform and low pressure drop spacer grid designs which should be informed by clear engineering principles. This would constitute further actions from the present findings. Also, taking into consideration varying flow velocities (varying Reynolds number), further quantitative study is required to find out optimum operating conditions for the different mixing spacer grid structures presented in this study.

Table 7
Comparison of mixing effect for quarter rod geometries.

Quarter Rod Geometry Gap	No Spacer grid	Spacer grid	Spacer grid with split vane	Spacer grid with swirl vane
Gap 1	−0.98	−0.34	3.29	3.01
Gap 2	−1.68	−0.73	3.46	3.21
Gap 3	0.67	0.93	2.52	2.19
Quantification of Mixing Effect	0.03	0.84	3.43	2.56

Table 6
Comparative Analysis of Rod Bundle Geometries.

Geometry	Velocity	Crossflow	TKE (Turbulent Intensity)	Turbulent Dissipation Rate (TDR)	Pressure drop
Spacer Grid + Swirl Vane	Good velocity mixing	Strong induced crossflow; persistent mid-stream mixing.	High TKE from swirl-induced turbulence.	Elevated dissipation with sharp peaks.	High pressure drops due to vane resistance.
Spacer Grid + Split Vane	Enhanced velocity redistribution; strong acceleration zones.	Moderate crossflow; less persistent than swirl vane.	Significant turbulence but lower than swirl vane.	Moderate dissipation; lower than swirl vane.	Moderate to high pressure drop; lower than swirl vane.
Spacer Grid Only	Velocity enhanced at grid location; flattens downstream.	Crossflow induced near grid; weaker overall.	Noticeable turbulence near grid.	Moderate dissipation localized around grid.	Moderate pressure drop due to spacer.
No Spacer Grid	More uniform velocity or laminar flow, lower redistribution.	Minimal crossflow and mixing.	Lowest turbulence intensity.	Lowest dissipation rates.	Lowest pressure drop.

Declaration of competing interest

The authors declare that they have no known competing financial interests or personal relationships that could have appeared to influence the work reported in this paper.

Data availability

Data will be made available on request.

References

Agbodemegbe, V.Y., Cheng, X., Akaho, E.H.K., Allotey, F.K.A., 2016. An investigation of the effect of split-type mixing vane on extent of crossflow between subchannels through the fuel rod gaps. Ann. Nucl. Energy 88, 174–185. https://doi.org/10.1016/j.anucene.2015.10.036.

Agbodemegbe, V.Y., Cheng, X., Akaho, E.H.K., Allotey, F.K.A., 2015. Correlation for cross-flow resistance coefficient using STAR-CCM+ simulation data for flow of water through rod bundle supported by spacer grid with split-type mixing vane. Nucl. Eng. Des. 285, 134–149. https://doi.org/10.1016/j.nucengdes.2015.01.003.

Chang, S.K., Kim, S., Song, C.H., 2014. Turbulent mixing in a rod bundle with vaned spacer grids: OECD/NEA-KAERI CFD benchmark exercise test. Nucl. Eng. Des. 279, 19–36. https://doi.org/10.1016/j.nucengdes.2014.05.013.

Conboy, T.M., McKrell, T.J., Kazimi, M.S., 2013. Experimental investigation of hydraulics and lateral mixing for helical-cruciform fuel rod assemblies. Nucl. Technol. 182 (3), 259–273. https://doi.org/10.13182/NT12-58.

Feldman, E. E. (2010). Steady-State Thermal-Hydraulic Analysis for Forced-Convective Flow in the Rhode Island Nuclear Science Center (RINSC) Reactor 1. 1–34.

Hainoun, A., Doval, A., Umbehaun, P., Chatzidakis, S., Ghazi, N., Park, S., Mladin, M., Shokr, A., 2014. International benchmark study of advanced thermal hydraulic safety analysis codes against measurements on IEA-R1 research reactor. Nucl. Eng. Des. 280 (June), 233–250. https://doi.org/10.1016/j.nucengdes.2014.06.041.

Irschik, H., Holl, H.J., 2015. Lagrange's equations for open systems, derived via the method of fictitious particles, and written in the Lagrange description of continuum mechanics. Acta Mech. 226 (1), 63–79. https://doi.org/10.1007/S00707-014-1147-8.

Kaptsov, E., Modelling, S. M.-A. M., & 2020, (2018). Analysis of the one-dimensional Euler–Lagrange equation of continuum mechanics with a Lagrangian of a special form. *Elsevier*. https://www.sciencedirect.com/science/article/pii/S0307904X1930544X.

Lee, J., Facchini, A., Joo, H.G., 2019. Development of a drift-flux model based core thermal-hydraulics code for efficient high-fidelity multiphysics calculation. Nucl. Eng. Technol. 51 (6). https://doi.org/10.1016/j.net.2019.04.002.

Lee, J., Lee, J.H., Park, H., 2020. Modified mixing coefficient for the crossflow between sub-channels in a 5 × 5 rod bundle geometry. Nucl. Eng. Technol. 52 (11), 2479–2490. https://doi.org/10.1016/J.NET.2020.05.002.

Lee, J.R., Kim, J., Song, C.H., 2014. Synthesis of the turbulent mixing in a rod bundle with vaned spacer grids based on the OECD-KAERI CFD benchmark exercise. Nucl. Eng. Des. 279, 3–18. https://doi.org/10.1016/j.nucengdes.2014.03.008.

Li, X., Chen, D., Hu, L., 2019. Numerical investigation on mixing performance in rod bundle with spacer grid based on anisotropic turbulent mixing model. Int. J. Heat Mass Transf. 130, 843–856. https://doi.org/10.1016/j.ijheatmasstransfer.2018.10.121.

Liu, A., Yang, B.W., Han, B., Zhu, X., 2020. Turbulent mixing models and other mixing coefficients in subchannel codes—a review part a: single phase. Nucl. Technol. 206 (9). https://doi.org/10.1080/00295450.2020.1792753.

Mao, H., Yang, B.W., Han, B., Liu, A., 2017. Modeling of spacer grid mixing effects through mixing vane crossflow model in subchannel analysis. Nucl. Eng. Des. 320, 141–152. https://doi.org/10.1016/j.nucengdes.2017.05.003.

Matozinhos, C.F., Tomaz, G.C.Q., Nguyen, T., Hassan, Y., 2021. Experimental investigation of turbulent flow characteristics in cross-flow planes of a 5×5 rod bundle with a spacer grid. Int. J. Heat Fluid Flow 87. https://doi.org/10.1016/j.ijheatfluidflow.2020.108757.

Möller, S.V., 1992. Single-phase turbulent mixing in rod bundles. Exp. Therm Fluid Sci. 5 (1), 26–33. https://doi.org/10.1016/0894-1777(92)90053-8.

Moorthi, A., Kumar Sharma, A., Velusamy, K., 2018. A review of sub-channel thermal hydraulic codes for nuclear reactor core and future directions. Nucl. Eng. Des. 332, 329–344. https://doi.org/10.1016/J.NUCENGDES.2018.03.012.

Pacio, J., Litfin, K., Batta, A., Viellieber, M., Class, A., Doolaard, H., Roelofs, F., Manservisi, S., Menghini, F., Böttcher, M., 2015. Heat transfer to liquid metals in a hexagonal rod bundle with grid spacers: Experimental and simulation results. Nucl. Eng. Des. 290, 27–39. https://doi.org/10.1016/j.nucengdes.2014.11.001.

Park, H., Kim, I.G., Lee, M.H., Jeong, Y.S., Bang, I.C., 2020. Study on the effects of flow-driven rotational mixing vanes by flow pattern tracking. Nucl. Eng. Des. 365. https://doi.org/10.1016/j.nucengdes.2020.110661.

Pioro, I., Duffey, R., 2019. Current status of electricity generation in the world and future of nuclear power industry. Manag. Global Warming: Interface Technol. Human Issues 67–114. https://doi.org/10.1016/B978-0-12-814104-5.00003-X.

Podila, K., Rao, Y.F., Krause, M., Bailey, J., 2014. A CFD simulation of 5 × 5 rod bundles with split-type spacers. Prog. Nucl. Energy 70, 167–175. https://doi.org/10.1016/j.pnucene.2013.08.012.

Qu, W., Xie, H., Shen, D., Wang, Z., Xiong, J., 2023. Experimental study of coherent structures downstream mixing vaned spacer grid of different inclination angles in a 5 × 5 rod bundle by TR-PIV. Ann. Nucl. Energy 181. https://doi.org/10.1016/j.anucene.2022.109516.

Ren, Q.Y., Zhou, W.X., Du, S.J., Li, Z.C., Pan, L.M., 2018. Sub-channel flow regime maps in vertical rod bundles with spacer grids. Int. J. Heat Mass Transf. 122. https://doi.org/10.1016/j.ijheatmasstransfer.2018.01.133.

Wang, S., Duan, W., Chen, X., Zhuang, K., 2021. CFD study on crossflow and heat transfer characteristics of single phase flow in rod bundle with spacer grid under rolling conditions. Prog. Nucl. Energy 137. https://doi.org/10.1016/j.pnucene.2021.103791.

Wang, Y., Wang, M., Ju, H., Zhao, M., Zhang, D., Tian, W., Liu, T., Qiu, S., Su, G.H., 2020. CFD simulation of flow and heat transfer characteristics in a 5×5 fuel rod bundles with spacer grids of advanced PWR. Nucl. Eng. Technol. 52 (7), 1386–1395. https://doi.org/10.1016/j.net.2019.12.012.

World Energy Outlook 2023 - Event - IEA. (n.d.). Retrieved September 1, 2023, from https://www.iea.org/events/world-energy-outlook-2023.

Xiong, J., Qu, W., Zhang, T., Chai, X., Liu, X., Yang, Y., 2020. Experimental investigation on split-mixing-vane forced mixing in pressurized water reactor fuel assembly. Ann. Nucl. Energy 143. https://doi.org/10.1016/j.anucene.2020.107450.

Zhang, X., Gui, N., Gong, H.J., Yang, X., Tu, J., Jiang, S., 2023. Thermal hydraulic review of light water reactor based on subchannel code CTF. Nucl. Eng. Des. 413. https://doi.org/10.1016/j.nucengdes.2023.112482.

Zhu, X., Morooka, S., Oka, Y., 2014. Numerical investigation of grid spacer effect on heat transfer of supercritical water flows in a tight rod bundle. Int. J. Therm. Sci. 76, 245–257. https://doi.org/10.1016/j.ijthermalsci.2013.10.003.